Estimation of Reflectance Properties of Small Solar System Bodies from Optical Remote Sensing

German Title: Abschätzung von Reflexionseigenschaften von Kleinkörperoberflächen aus optischen Fernerkundungsdaten

by **Peter Dorman**

A thesis presented for the degree

Bachelor of Science

1st Examiner:	Dr. Marco Scharringhausen
	Deutsches Zentrum für Luft- und Raumfahrt (DLR)
2nd Examiner:	Prof. Dr. rer. nat. Claus Lämmerzahl
	Zentrum für angewandte Raumfahrttechnologie und Mikrogravitation (ZARM)

Diese Erklärungen sind in jedes Exemplar der Abschlussarbeit mit einzubinden.

Name:_____ Matrikel-Nr.: _____

Urheberrechtliche Erklärung

Erklärung gem. § 10 (10) Allgemeiner Teil der BPO vom 27.10.2010

Hiermit versichere ich, dass ich meine Bachelorarbeit ohne fremde Hilfe angefertigt habe, und dass ich keine anderen als die von mir angegebenen Quellen und Hilfsmittel benutzt habe.

Alle Stellen, die wörtlich oder sinngemäß aus Veröffentlichungen entnommen sind, habe ich unter Angabe der Quellen als solche kenntlich gemacht.

Die Bachelorarbeit darf nach Abgabe nicht mehr verändert werden.

Datum: _____ Unterschrift: _____

Erklärung zur Veröffentlichung von Abschlussarbeiten

Bitte auswählen und ankreuzen:

- o Ich bin damit einverstanden, dass meine Abschlussarbeit im Universitätsarchiv für wissenschaftliche Zwecke von Dritten eingesehen werden darf.
- o Ich bin damit einverstanden, dass meine Abschlussarbeit nach 30 Jahren (gem. §7 Abs.2 BremArchivG) im Universitätsarchiv für wissenschaftliche Zwecke von Dritten eingesehen werden darf.
- o Ich bin nicht damit einverstanden, dass meine Abschlussarbeit im Universitätsarchiv für wissenschaftliche Zwecke von Dritten eingesehen werden darf.

Datum: _____ Unterschrift: _____

Contents

1 Motivation **3**

2 Aim of study **4**

3 Introduction **4**

3.1 Small Solar System Bodies & Dwarf Planets 4

3.2 Asteroids 5

3.2.1 C-type asteroids 6

3.2.2 S-type asteroids 6

3.2.3 V-type asteroids 6

3.3 Small Body & Dwarf Planet Missions 9

3.3.1 DAWN 9

3.3.2 Other Missions 12

4 Methodology **14**

4.1 Coordinate Systems, Time & *SPICE* 14

4.2 Reflectance and Hapke-Model 15

4.3 Illumination & Camera Simulation 17

4.4 Optimization 17

4.5 Inverse Problems 22

4.6 Solar Irradiance 23

5 Results **24**

5.1 Coordinate Calculation 24

5.2 Vesta Results 24

5.3 Ceres Results 31

6 Conclusion & Outlook **33**

1 Motivation

Asteroids and small bodies of the solar system are subject to research for many space missions. Very popular was the recent *Rosetta* Mission to 67P/Churyumov–Gerasimenko, which for the first time brought a lander (*Philae*) to land on a comet. Also, the mission *New Horizons* examined the dwarf planet Pluto and captured the first high resolution images of it. Furthermore, the *DAWN* mission visited for the first time two asteroids in one mission, Vesta and Ceres. For the future exploration NASA announced the asteroid redirect mission with the attempt to capture an asteroid and insert it into a lunar orbit. Due to vast differences in size, mass and composition, all bodies underlie different physical constraints. In this work the reflectance properties of the small bodies Vesta and Ceres in the asteroid belt are examined. Due to the gravitational influence of Jupiter, Vesta and Ceres represent bodies that could not accumulate enough mass to form a planet in the early development of the solar system. Therefore, they are ideal candidates to gain more information about planet development. The reflectance properties however are basic properties in a scientific process, which can lead to a better understanding of the chemical composition of the surface. A main topic of research is the search for water in the solar system and the surface properties of an object can indicate to the existence of liquid water or ice on the surface. It is also possible to deduce from the surface properties whether the object is solid or only loosely bound by gravity.

2 Aim of study

The general idea of this work is to create simulated pictures of Vesta and Ceres and to minimize the difference in brightness named Z for each pixel from the real picture taken by DAWN. The reflectance distribution is simulated in a Hapke-model and relies on four parameters (Single-Scattering Albedo (SSA) ω, scattering parameter g, and two Hot-Spot parameters B_0 and h). The correct parameters are extracted by minimizing the Z-function. The model uses a single-term Henyey-Greenstein phase function and no surface roughness parameter. The real pictures are calibrated Level-1b-images. Finally, the results are compared to results of other works and discussed.

3 Introduction

3.1 Small Solar System Bodies & Dwarf Planets

The solar system consists of many different objects of mass. But not only the mass, but also shape, gravitational influence, sun distance or sun orbit can be a valid reason for objects to belong to a category. However, to cover all bodies of the solar system, these four categories can be used: [31]

- Planets
- Dwarf planets, like Pluto or Ceres
- Small Bodies, like Vesta or Churyumov-Gerasimenko
- Satellites, more commonly known as moons

By definition a planet is spherical due to its own gravity, orbits the sun and has cleared its orbit around the sun of other objects. This definition was made by the International Astronomical Union in 2006 following discoveries of many Trans-Neptunian objects (TNOs). Until then the solar system had nine planets. After the new definition however, Pluto was not considered a planet anymore, it now is considered a dwarf planet.
A dwarf planet has not cleared its orbit around the sun from other objects but still has the spheric form due to its gravity. As Pluto orbits the sun but not as the only object, it cannot be defined as planet. This makes sense, as there are few TNOs similar to Pluto.
A small body is irregular shaped and orbits only the sun. The most well-known small bodies are asteroids and comets. These usually have a highly elliptical orbit around the sun but differ in composition. Comets usually form in the outer solar system and are mostly made of ice and rock. The ice is the reason why they are visible when they come close to the sun: They melt.
Asteroids can be found in different parts of the inner solar system.
A satellite orbits a planet, dwarf planet, or small body. Earth is orbited by the Moon, Mars by Phobos and Deimos, and Jupiter by over 60 satellites.
There are many more definitions for solar system bodies based on size, composition or location (see figure 1).

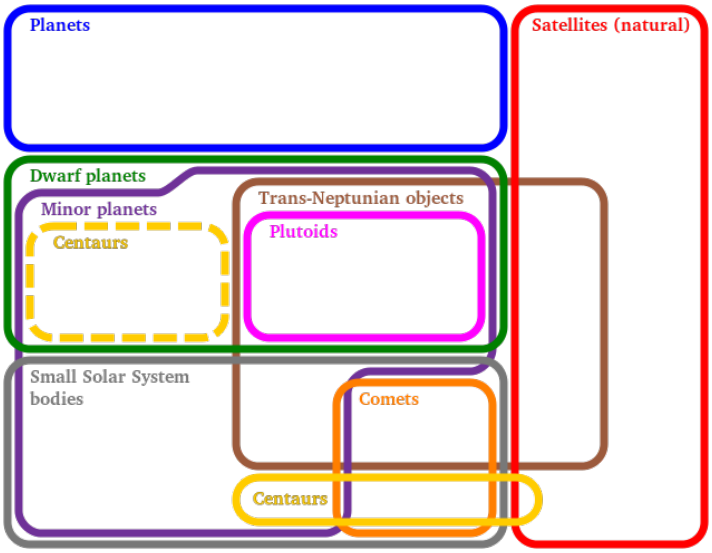

Figure 1: Euler-Diagram showing borders of categories for solar system bodies (Reprint from [29])

3.2 Asteroids

Asteroids are small rocky bodies in the inner solar system. The highest density of asteroids can be found in the asteroid belt between Mars and Jupiter with an estimate of at least a billion asteroids. The size of asteroids varies strongly from a few centimetres to a few hundred kilometres in diameter. Most asteroids are very small and therefore, the total mass of the asteroid belt is estimated to be about 5% the mass of the Moon. The reason for the asteroids to remain is this area is the constant gravitational influence of Jupiter, the most massive planet in the solar system. Its gravitational pull made the formation of another terrestrial planet in this area impossible. The word "belt" is in this case only useful to a certain extent. There are many more asteroids here than anywhere else in the inner solar system. However, most of the space is empty. Statistically, the mean seperation between asteroids larger than 1 km is roughly 3 million kilometres. The two largest objects in the asteroid belt are Ceres and Vesta.
The composition and general reflectance properties of asteroids vary. The classification by Tholen [30] distinguishes between 14 different types of which the main four groups are:

- C-group (carbonaceous)
- S-type (slilicaceous)
- X-group (metallic)
- small classes

We will focus in this work on Vesta (small class, V-type) and Ceres (C-group, G-type), however the predominant types are presented at this point. The wavelength dependant spectra of some asteroids are presented in figure 4.

Figure 2: C-type asteroid 253 Mathilde [23]

3.2.1 C-type asteroids

These types can be usually found in the outer part of the asteroid belt. The outstanding feature of C-types is the very dark surface, which is due to a high amount of carbon in the composition. The geometric albedo lies in the range $\omega_{geo} = 0.03 - 0.09$ [18]. The composition is in general similar to the sun, except for hydrogen and helium. About 75% - 80% of all asteroids can be classified as C-type. A typical C-type asteroid can be seen in figure 2.

3.2.2 S-type asteroids

S-types can be found mostly in the inner asteroid belt and are made of metallic iron mixed with iron- and magnesium-silicates. They have higher geometric albedos and acccount for 17% of all asteroids. The albedo usually lies in a range of $\omega_{\text{geo}} = 0.10 - 0.22$ [18]. A typical S-type asteroid can be seen in figure 3.

3.2.3 V-type asteroids

As the main focus of this work lies on 4 Vesta, the V-type (also: "Vestoid") shall be considered. These types are very bright and have fairly similar composition to S-types. The main difference is a greater amount of pyroxene in V-types. These types have supposedly formed during a large cratering event on Vesta about 1 billion years ago [14].

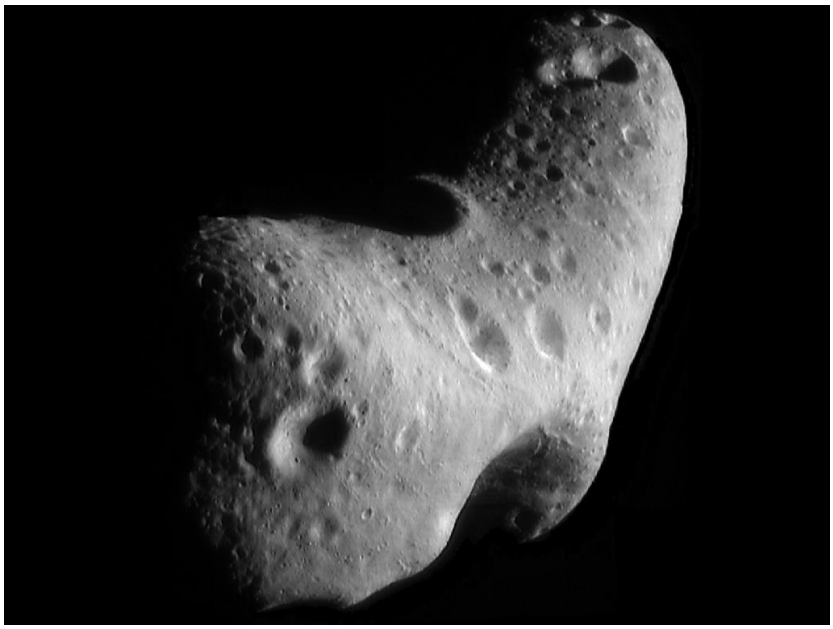

Figure 3: S-type asteroid 433 Eros [20]

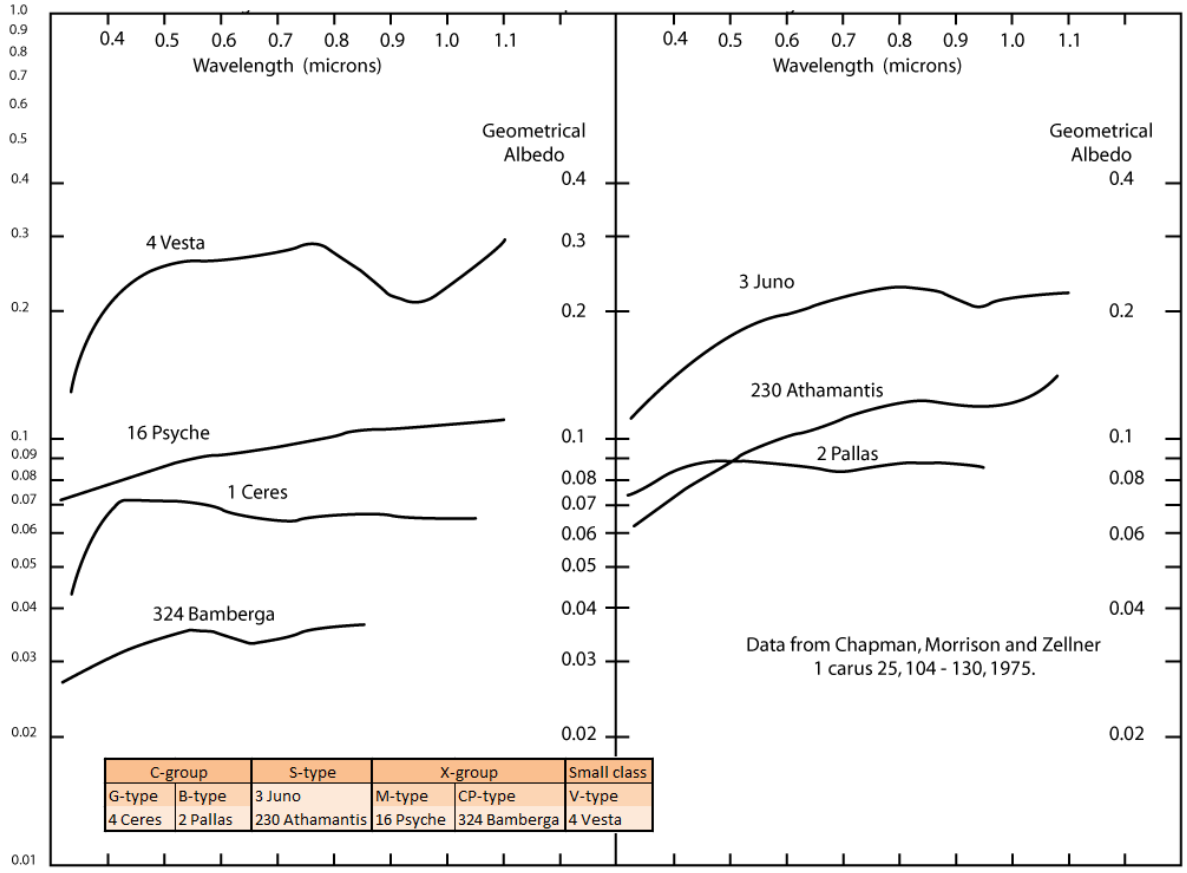

Figure 4: Spectra of different asteroids. Data from [2], reprint from [24]

1 Ceres

1 Ceres was first spotted in 1801 by Giuseppe Piazzi. It underwent a series of changes in classification. Originally classified as a planet by Piazzi, it was reconsidered an asteroid by John Herrschel just one year later. By 1850 about 14 similar objects were found in the region of the then introduced term "Asteroid Belt". With the demotion of Pluto 2006 and the new category "dwarf planet", the official status of Ceres changed again and it is now classified as dwarf planet as well. Additionally, it is still considered an an asteroid. The main reasons for this are the composition, spectral type and location in the asteroid belt.
Ceres is the largest object in the asteroid belt with a radius of 476 km and needs 4.6 years to revolve the sun at an average distance of 413 million km. It is the only dwarf planet without a moon. The inner core of Ceres is probably solid, above that lies a mantle of water ice. It is possible that Ceres holds up to 25% water, which would be more than Earth holds. Due to its location in the asteroid belt Ceres' surface is scattered with craters. The biggest one is 280 km in diameter.

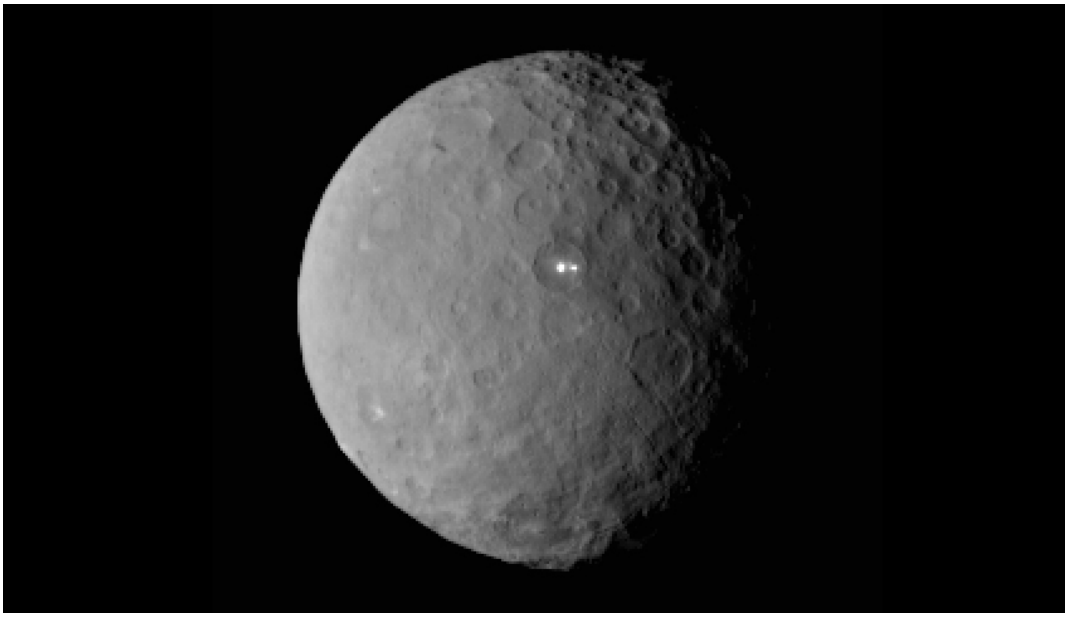

Figure 5: Asteroid Ceres [22]

4 Vesta

4 Vesta is the second largest and second most massive asteroid. It is almost spherical not quite making it as a dwarf planet. It was discovered 1807 by Bremen-born astronomer Heinrich Wilhelm Olbers.
Despite not being a planet or dwarf planet it shows planet-like features like the separation of an inner core, a mantle and a crust. It formed about 1-2 million years into the existence of the solar system. The surface has a wide range in brightness. The parts of the surface that appear brighter are considered to be native rocks, whereas the dark parts are the remains of other asteroids crashing into Vesta. It is the brightest asteroid and can under the right circumstances theoretically be seen with the naked eye

from Earth as it peaks around mag.5.4 [17] [25].

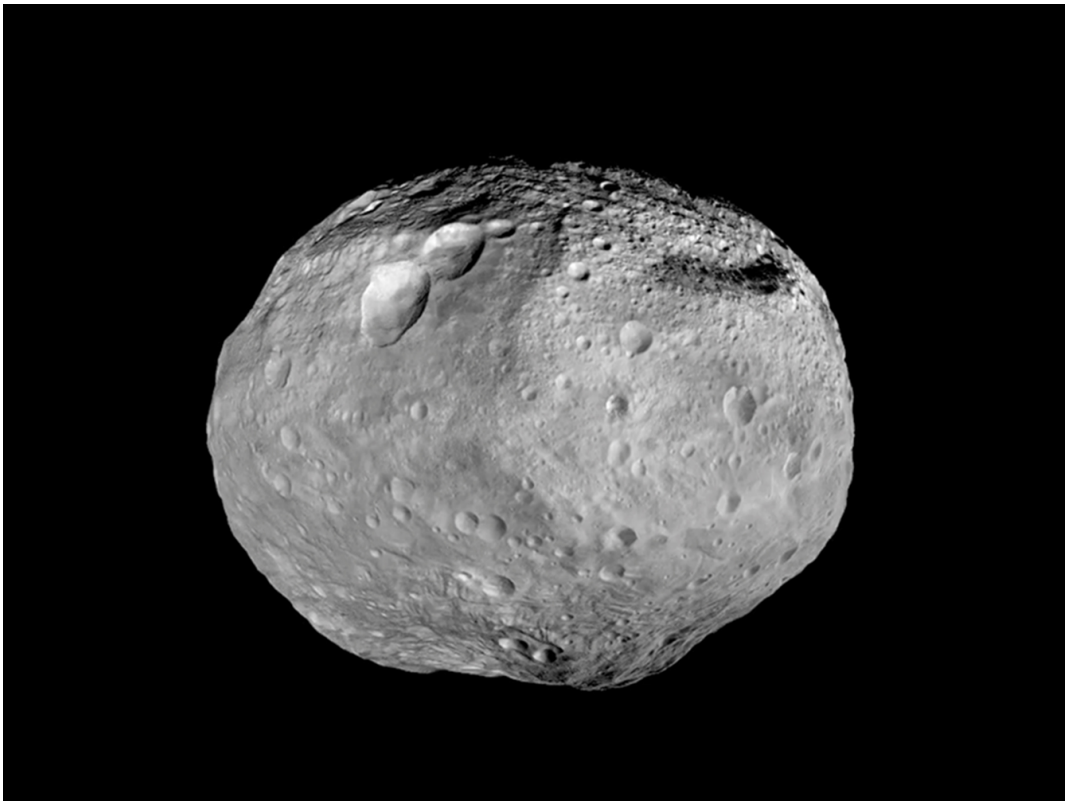

Figure 6: Asteroid Vesta [21]

3.3 Small Body & Dwarf Planet Missions

3.3.1 DAWN

The Dawn mission by NASA was launched in September 2007 with the objective to visit the asteroids Ceres and Vesta, being the first mission to visit two asteroids in one mission. The main scientific question that DAWN's data is meant to answer is the role of size and water in the evolution of planets. Ceres and Vesta are perfect candidates, as they are both asteroids but differ strongly in their physical properties.

Mission timeline

After the 2007 launch from Cape Canaveral Air Force Station, Florida, it passed Mars in February 2009 and arrived at Vesta in July 2011. From 2nd August DAWN orbited Vesta at an altitude of 2750 km, also known as *Survey* orbit. On 27th September DAWN entered a High-Altitude Mapping Orbit (*HAMO*) at an altitude of 680 km and on 8th December at an altitude of 210 km a Low-Altitude Mapping Orbit (*LAMO*) (see figure 8). DAWN departed from Vesta in September 2012.

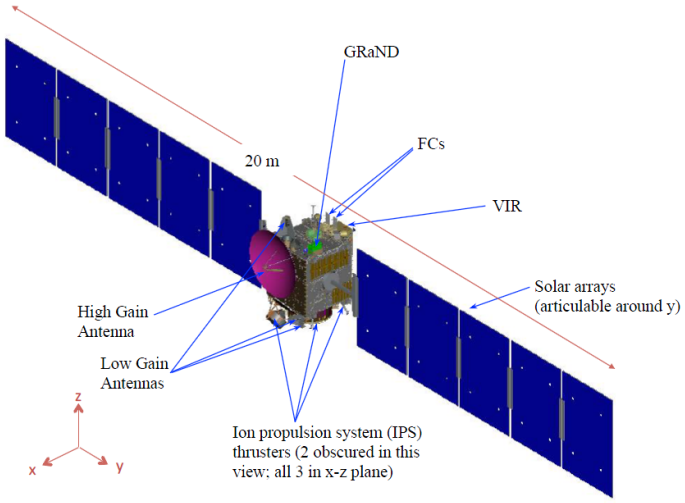

Figure 7: DAWN spacecraft with instruments and reference frame (Reprint from [7])

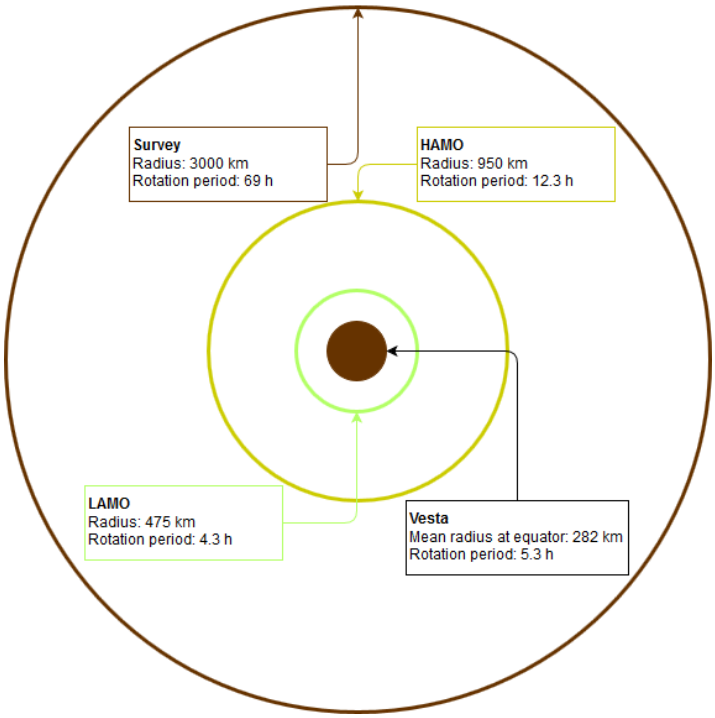

Figure 8: Observing Orbits of DAWN at Vesta

Parameter	FC
Focal Length (mm)	150.0
Aperture (mm)	19.9
f/ratio	f/8
IFOV (microrad/pixel)	93.3
Field of view (degree)	
Cross-track	5.46
Along-track	5.46

Table 1: Optical parameters of the Framing Cameras. Data from [27]

On 6th March 2015 DAWN was inserted into a Ceres orbit. Until today (21st August 2017) the Mission is still active and orbiting Ceres on an elliptical trajectory. There are currently no further objectives and the mission is estimated to last until 2018 until the resources for the propulsion system are used up.

Instruments

The spacecraft carries three instruments for scientific research [4]:

FC The Framing Cameras

VIR The Visual and Infrared Spectrometer

GRaND The Gamma Ray and Neutron Detector

Framing Camera

DAWN carries two identical Framing Cameras for redundancy. It includes a clear filter and 7 band-pass filters. The covered wavelengths range from 400-1050 nm, which means that the camera covers the complete visible spectrum and some near infrared (NIR). Scientific objectives include:

- Determine origin, evolution, shape and volume of the asteroids
- Measure the spin rate and pole position
- Map the topography and the basic mineralogical composition

The cameras are used for orbit navigation in addition to their scientific purpose. The highest resolution of Vesta lies at 12m/pixel in LAMO and 62m/pixel at Ceres. The boresight of the cameras point in the Z-direction of the instrument and spacecraft frame. To take pictures in a specific wavelength a filter can be used. The filters are aligned in a filter wheel and have different characteristics (fig. 9). The exposure time varies and can be set to values in a range of $1\text{ms} - 3.5\text{h}$. For Survey and Approach, exposure times around 400ms were chosen. Additional data about the optics can be found in table 1. The camera itself is based on a CCD with a light-sensitive area of 1024x1024 pixels. To protect the camera from direct solar radiation and volatiles, a door mechanism is used. Whenever the camera is not in use, the door is closed.

Image Processing

The CCD converts the arriving irradiance in electrical charge. From this the irradiance has to be recalculated taking into account bias, dark current and flat-field non uniformity. The data produced with these calibrations is called Level 1b data. This kind of data is used in this work. A higher calibration (Level 2) includes georeferencing, orthorectification, mosaicking and photogrammetric analysis. A lower level (Level 1a) contains unprocessed values between 0 and 16383 DN. [28]

3.3.2 Other Missions

Rosetta was a mission between 2004 and 2016 by the European Space Agency (ESA) to the comet 67P. 2014 it arrived at the comet and deployed the comet lander Philae. Its main goals were amongst others to characterize the nucleus, determine the dynamic properties, surface morphology and composition. For these purposes Rosetta carried 11 scientific instruments plus 10 scientific instruments on lander Philae. New in this mission was that the lander actually had a soft landing instead of crashing into the surface. The lander gained data about the surface but had to go into hibernation due to an unforeseen landing site without direct sunlight. [6]

New Horizons is a mission that launched in 2006. In 2015 it passed Pluto and took the first high resolution images of it. It was not possible for New Horizons to join a Pluto orbit due to the high velocity of the space probe. The aim of the mission is to get a better understanding of the outer solar system, mainly the Kuiper Belt, and how the objects of mass like Pluto formed and evolved. The exploration of the Kuiper Belt is currently ranked of the highest priority for solar system exploration by the National Academy of Sciences. Due to financial uncertainty the future of the mission with a continuing study of the Kuiper Belt is unknown. [19]

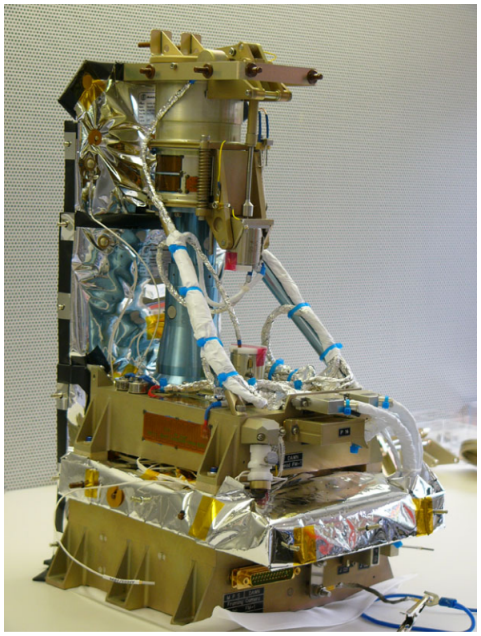

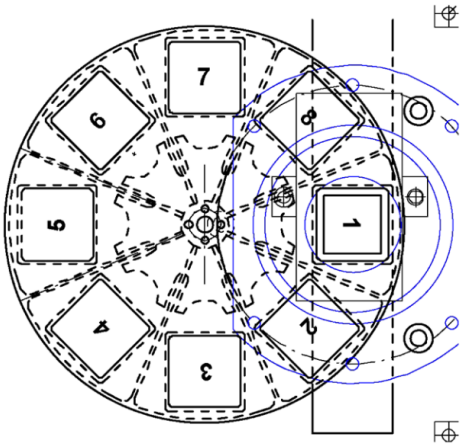

Channel No.	Center wavelength [nm]	Bandwidth [nm]	Transmission [%]	Filter-wheel position	Thickness [mm]
1	polychromatic	450 ± 10 to 920 ± 10	98	F1	6.00 ± 0.05
2	430 ± 2	40 ± 5	>75	F8	2.00 ± 0.05
3	550 ± 2	40 ± 5	>75	F2	5.90 ± 0.05
4	650 ± 2	40 ± 5	>75	F7	6.60 ± 0.05
5	750 ± 2	40 ± 5	>75	F3	6.40 ± 0.05
6	830 ± 2	40 ± 5	>75	F6	5.90 ± 0.05
7	920 ± 2	40 ± 5	>75	F4	5.30 ± 0.05
8	980 ± 2	80 ± 5	>75	F5	4.80 ± 0.05

Figure 9: DAWN Framing Camera without insulation (top left), filter wheel mechanism (top right), and filter specifications (bottom) (all reprints from [28])

4 Methodology

4.1 Coordinate Systems, Time & *SPICE*

To calculate the correct position and orientation of the spacecraft, it is necessary to understand the definition of coordinates and time. In space it is crucial to define time and space accordingly to allow calculations to be correct.

Time

For correct calculation the exact time is a key setting. In this work Universal Time (UTC) was used as well as Ephemeris Time (ET). UTC is commonly used all around the world and relies on Earth's position towards the sun. ET is given in seconds past the J2000 epoch. This is more general and more commonly used for spacecraft missions.

Spatial reference frames

A reference frame is necessary in the solar system as the movements of the bodies within can be only evaluated in relation to each other. It defines the orientation of the axes. A reference frame differs from a coordinate system as a coordinate system uses the axes of the reference frame but assignes values to the axes. It can be distinguished between Inertial and Non-Inertial reference frames. Inertial reference frames are, for example, the J2000 and Eclip J2000 system, in which the reference frames are defined with the plane of the celestial equator (J2000 frame), respectively the ecliptic plane at the J2000 epoch. This definition is needed because even the celestial equator and ecliptic are changing in the course of time.
Non-Inertial reference frames are changing in the course of time. The coordinate origin usually lies in a moving body and the orientation of the axes are a function of time. The reference frames used in this work for that instance are:

- Vesta-fixed frame (see table 2)
- Ceres-fixed frame
- DAWN frame (see figure 7)

There are four different coordinate systems used with Vesta which all define the prime meridian differently. Table 2 shows the definition of the coordinate systems accordingly.

	Pole RA	Pole Dec	Wdot	W0	Olbers Regio (lat, lon)	Claudia Crater (lat, lon)	PCK File
IAU-2000	301.0º	41.0º	1617.332776	292.0	+10º, 0º	+4.3º, 145.0º	dawn_vesta_v01.tpc
Dawn-Claudia	309.031º	+42.235º	1617.3329428	75.39º	+11º, 210º	-1.6º, 356.0º	dawn_vesta_v04.tpc
Claudia Prime				295.39º	+11º, 350º	-1.6º, 136.0º	dawn_vesta_v05.tpc
Claudia Double-Prime				285.39º	+11º, 0º	-1.6º, 146.0º	dawn_vesta_v06.tpc

Table 2: Coordinate Systems of Vesta as defined in the PCK files. Reprint from [12]

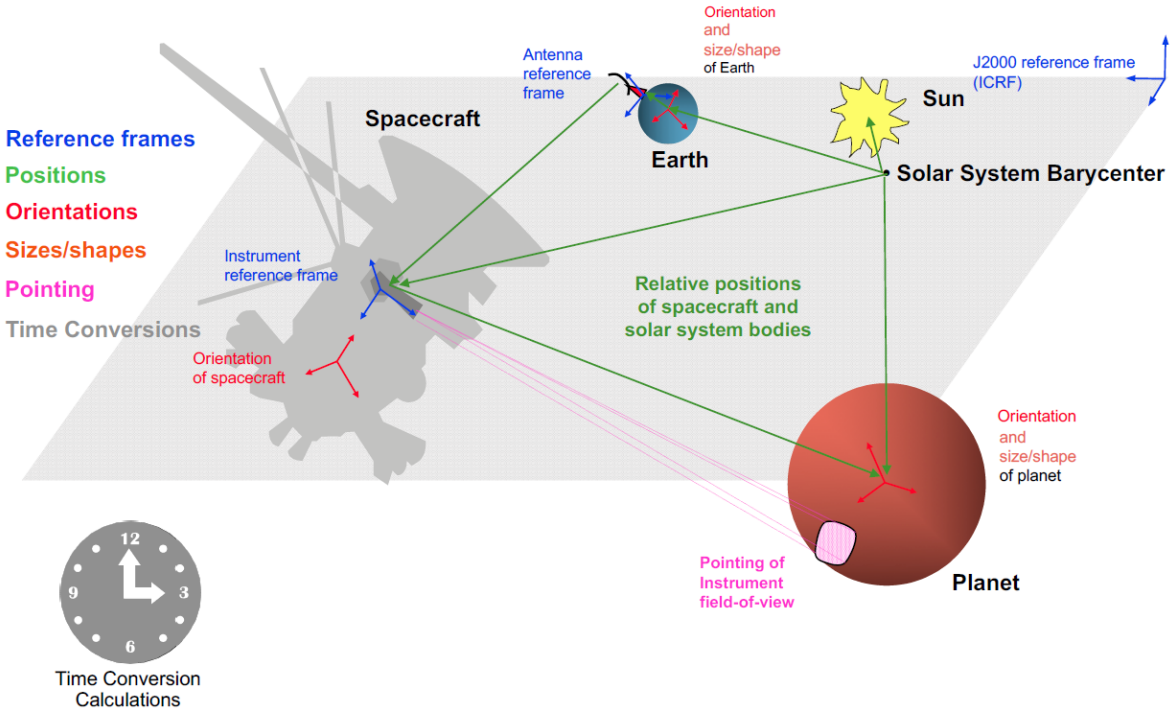

Figure 10: Reference frames and data saved in SPICE kernels visualized (Reprint from [16])

SPICE

The calculations were done with Mice, the Matlab toolkit extension of SPICE. It provides the user with Matlab commands to calculate all kind of position data, speed data, field-of-view data and many more. It is issued by the Navigation and Ancillary Information Facility (*NAIF*) and described as "An Observation Geometry System for Space Science Missions" [15].
Data is stored in so-called kernels and split up into several groups. This allows the user to load only the data necessary for his calculation. The kernels for many NASA-missions as well as generic kernels are openly accessible via the Planetary Data System (PDS). Figure 10 shows how different reference frames work and table 3 shows the different storage of data in different kernels.

For position calculations a reference frame, coordinate system, time and center of the coordinate system have to be given. Then subroutines included in the toolkit can be used for the calculation of position and velocity. Also, light time correction and stellar aberration can be included in the calculation. Another subroutine can be used for calculating transformation matrices for coordinate system transformation.

4.2 Reflectance and Hapke-Model

All celestial bodies (except the Sun) in the solar system are in the visible spectrum due to their reflectance of sunlight. The bodies without atmosphere share some properties, as the light reflects directly of the surface without interfering with gases or liquids. Bruce Hapke developed a model to

Kernel type	Content
SPK	Position of spacecraft and celestial bodies (ephemerides)
PcK	Size, shape and other constants of celestial bodies
IK	Shape, field-of-view, orientation and optional addition information
CK	Attitude and orientation of a spacecraft or artificial satellite
EK	Different components of additional events
FK	Definition of and relation between reference frames
LSK	Tabulation of leap seconds for time conversion
SCLK	Specifications about the spacecraft clock for time conversion
DSK	Shape model of spacecraft or celestial bodies

Table 3: Kernel types of SPICE

predict the reflectance properties of these non-atmospheric solar system bodies. It takes into account non-isotropic scattering as well as hot spots and relies on four parameters, which are:

$\boldsymbol{\omega}$ the single-scattering albedo

$\boldsymbol{g}$ the Henyey-Greenstein scattering parameter

$\boldsymbol{B_0}$ the hot spot height

$\boldsymbol{h}$ the hot spot angular width

The Hapke model used in this work is a simplified version without surface roughness with a Bidirectional Reflectance Distribution Function p:

$$p = \frac{\omega\mu_0}{4(\mu_0 + \mu)} \cdot \Big\{ P(\alpha, g)[1 + B(\alpha, h, B_0)] + H(\omega, \mu)H(\omega, \mu_0) - 1 \Big\} \tag{1}$$

In this equation α is the phase angle, μ_0 is the cosine of the incidence angle and μ is the cosine of the emission angle. Multiplied by the solar irradiance arriving at the body (1) can be used to calculate the reflected intensity. The entire theoretical background to this theory can be found in [8]. In this equation $H(\omega, x)$ is approximated as

$$H(\omega, x) = \frac{1 + 2x}{1 + 2x\sqrt{1 - \omega}} \tag{2}$$

$B(\alpha)$ defines the hot spots as

$$B(\alpha) = \frac{B_0}{1 + \tan(\alpha/2)/h} \tag{3}$$

The implemented Henyey-Greenstein phase function $P(\alpha, g)$ is

$$P(\alpha, g) = \frac{1 - g^2}{[1 + g^2 - 2g\cos(\alpha)]^{3/2}} \tag{4}$$

with $-1 < g < 1$ [10]. This function defines non-isotropic scattering. A parameter $g < 0$ indicates predominantly backscattering, $g > 0$ indicates predominantly forward scattering.

The closest and therefore strongly examined celestial body to Earth is the Moon. Interestingly the brightness seems to rise disproportionately at full moon. This is scientifically studied and the intensity of reflected light of the moon is significantly higher during full moon. This is called the opposition effect. There are two widely accepted explanations for this effect:

- During full moon the phase angle between earth and sun is 0°, hence the visible part is entirely lit by sunlight. Therefore, even in the small structures of the surface no shadows can be seen. The amount of shadows increases drastically with the phase angle. This explanation is called the Shadow-Hiding Opposition Effect (SHOE).
- The particles on the surface usually do not scatter the light isotropically. At low phase angles the light scattered back at the observer interferes more frequently constructively and causes a rise in brightness. This explanation is called the Coherent Backscatter Opposition Effect (CBOE).

This effect has been found not only on the moon, but on all other non-athmospheric bodies as well.

4.3 Illumination & Camera Simulation

The only source of radiation in the simulation is the sun. The sun rays are simulated using raytracing. The object to be illuminated has do be in form of a triangular 3D-grid. At the beginning of a calculation a user-defined amount of boxes is defined to cover the simulated area. For each ray it is tested whether the ray hits a box with triangles or not. If not, the next box is tested until a box with triangles is reached . Then the triangles are tested for intersection in that box. The first intersection of a ray with a triangle means the triangle is daylit. The second intersection can then be defined as night and the third intersection as shadow. In this version, only direct radiation is considered, which means that a triangle in the shadow cannot be illuminated by reflected light of a daylit triangle (see fig. 11).
The illumination simulation then assigns every triangle a value in brightness. Necessary inputs are the direction of sunlight in relation to the object and the maximum irradiance arriving at the object.

The camera simulation works very similar to the illumination simulation but "backwards". For each pixel the origin of the ray is determined and the reflectance according to the in 4.2 presented Hapke-model is calculated. The simplification here is that only one triangle accounts for the intensity arriving at the camera. Effectively, the camera is simulated as a pinhole camera. Necessary inputs are the amount of pixels, the focal length, the viewing angle and the camera orientation.
The key for the further remote sensing analysis is the included Hapke-Model. Once the body is illuminated, the Hapke parameters are assigned and a snapshot can be taken (figure 12).

4.4 Optimization

In the optimization process the pixels of the real and simulated pictures are compared in brightness. Mathematically it can be described as

$$Z = \sum_i |F_{Sim_i} - F_{Real_i}|^2 \tag{5}$$

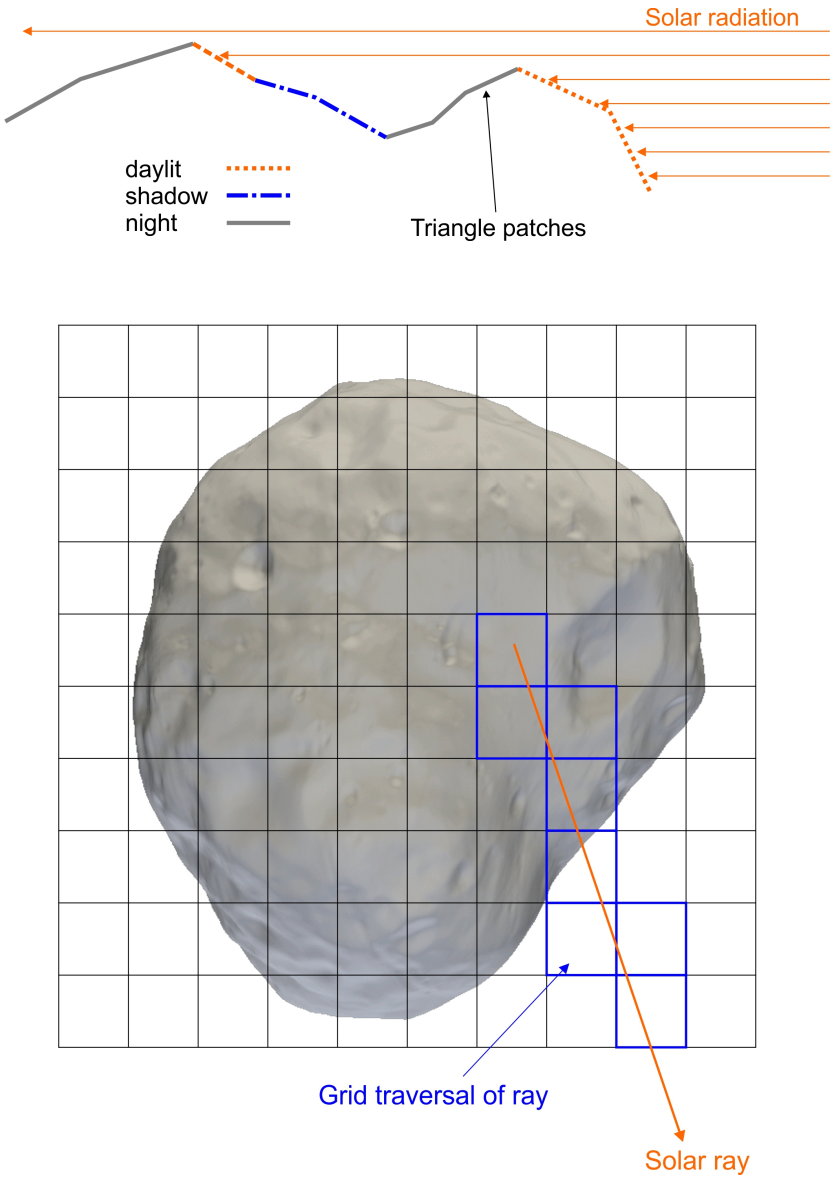

Figure 11: Illumination simulation using grids(boxes) and raytracing

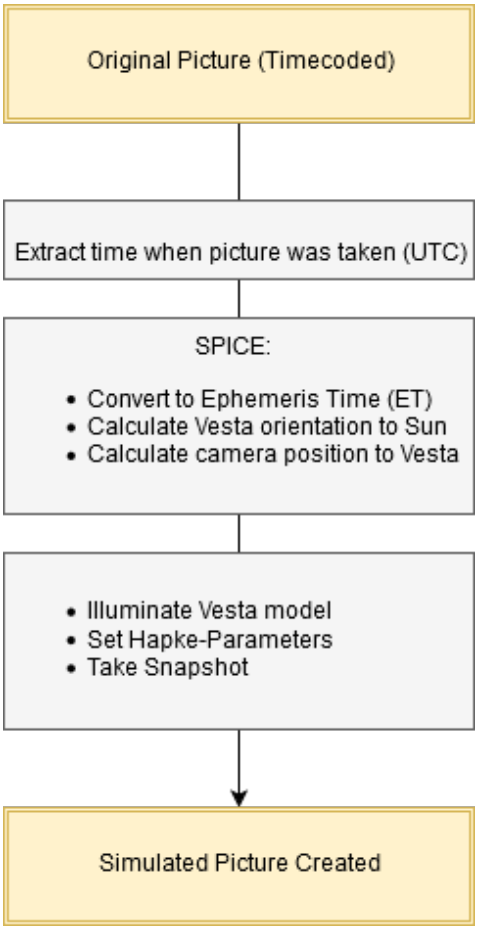

Figure 12: Process of creating a simulated Vesta picture

F_{Sim} is the simulated picture as a 1024x1024 greyscale matrix. F_{Real} is the real picture as a 1024x1024 greyscale matrix as this is the resolution of the Framing Camera. The value of a pixel is the flux received at the camera due to the Level-1-b data. Therefore, Z is the sum of difference for all pixels. This sum has to be minimized for the simulated picture to be as close to the real picture as possible. As F_{Sim} is a result of the implemented Hapke-Model, the Hapke-Parameters w, g, B_0 and h have to be altered in the optimization process.

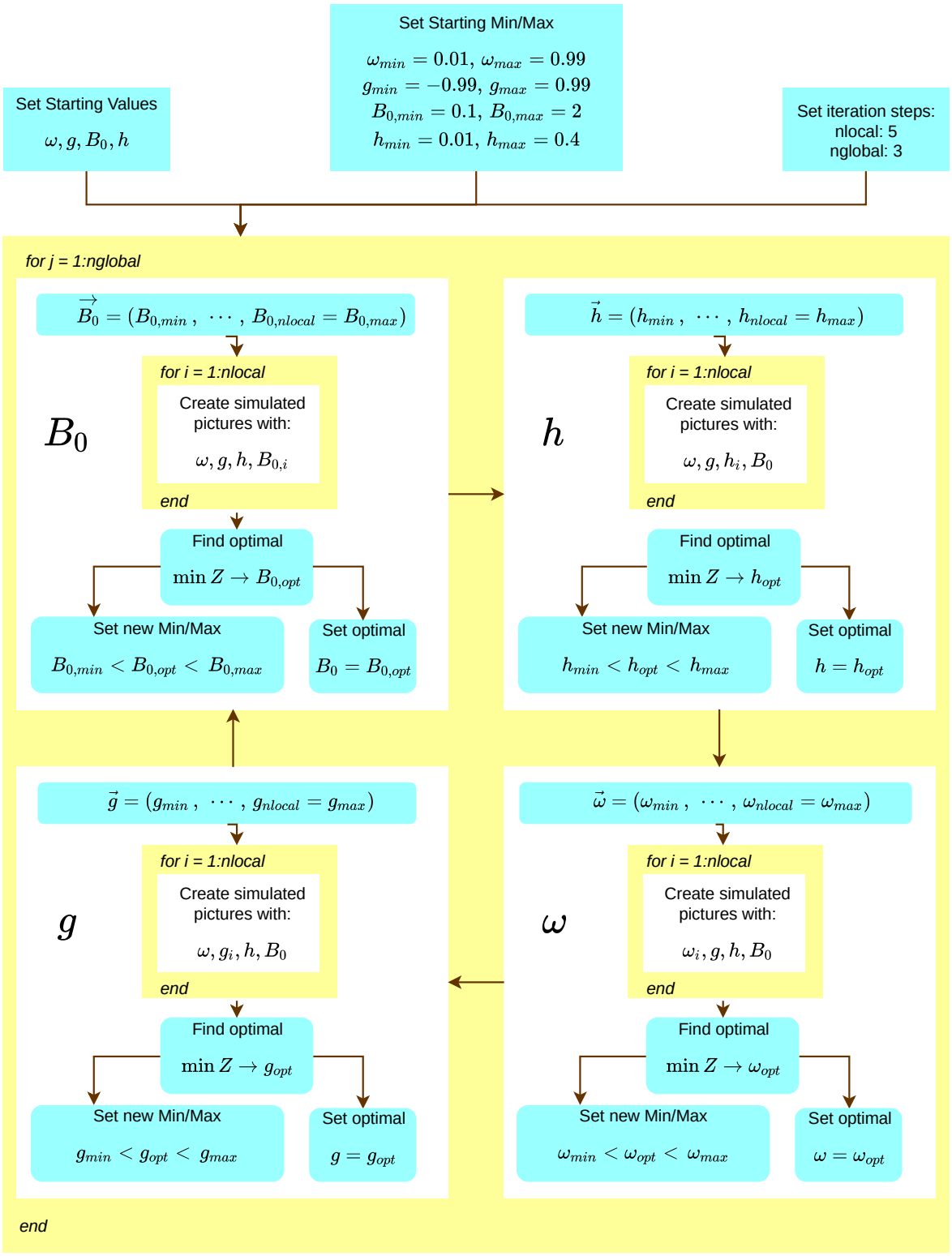

Figure 13: Optimization process of Hapke-Parameters

Optimizing Hapke-Parameters

A widely used method for optimization problems like these is the gradient method. By calculating the gradient of a multidimensional function the direction of the steepest descent can be found until a minimum is reached. The disadvantage of this method is that many steps have to be made to reach the minimum. The reason it is unsuitable for this work is that each step contains a calculation of four complicated derivatives as well as a simulation of the light reflected off a body. All of this contributes to a very high calculation time. The method used instead is much simpler. Only one parameter at a time is altered in a specific range and the value of Z registered. After this is done for all parameters it is repeated for twice over. The result is not necessary a minimum of the function Z but manages to lower the value of Z significantly. This method also allows only certain parameters to be optimized, which can be especially useful if the other parameters are already known.

4.5 Inverse Problems

The more common problems occurring in Physics are forward problems. In these, parameters are known, a model is used and the outcome can be predicted and calculated. However, sometimes the parameters for the model are not known. Instead, the final outcome is known and the parameters are to be found. This is called an inverse problem. The difficulty here lies in the fact, that sometimes different parameters in the original models can lead to the same result.
This is not a very mathematical way of defining these kind of problems. A better more general definition can be given with the so-called well-posedness. A problem is defined well-posed if[5]:

- For all admissible data, a solution exists.
- For all admissible data, the solution is unique.
- The solution depends continuously on the data.

Data can be thought of as the input of a problem, *solution* as the output. Most important is the third property. It means that there is stability to the problem and makes it possible for slightly different inputs to receive only slightly different outputs [1]. In other words, the problem is independent of the starting values. A problem that does not fit these criteria is called ill-posed and can usually be seen as an inverse problem to a well-posed forward problem. An example for the difference between a forward problem and an inverse problem is numerical differentiation and numerical integration. Integration is a forward problem. The reason for this is its resistance to noise. Let $f(x)$ be our function and $n(x) << f(x)$ our random noise. This means that

$$\int f(x)dx = F(x) \approx \int \big(f(x) + n(x)\big)dx$$

The noise is cancelled out in this case, which means that the integration is very stable and noise-resistant. The inverse problem to this is the differentiation. This problem is ill-posed, as the problem is very unstable to noise.
In this work, the finding of the Hapke-Parameters is the inverse problem.

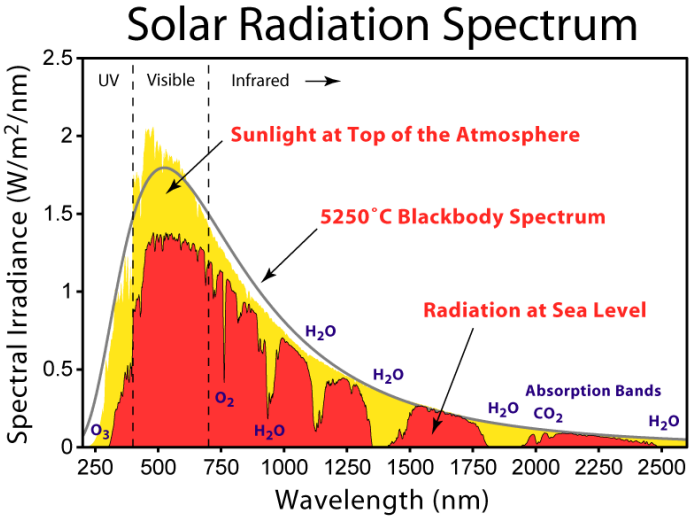

Figure 14: Solar spectrum compared to black body spectrum

4.6 Solar Irradiance

Irradiance in Physics is usually named Intensity. The solar irradiance measured at the top of the atmosphere averages annually at 1361 W/m^2. For the objects Vesta and Ceres no reliable sources of data for the solar irradiance exist. Therefore the irradiance has to be estimated and approximated by a model. The wavelength spectrum of the irradiance lets us approximate the sun as a black body with a temperature of 5700 K (fig. 14). The total irradiance H_{Sun} at the sun is given by the Stefan-Boltzmann law:

$$H_{\text{Sun}} = \sigma T^4 \cdot 4\pi R_{\text{Sun}}^2 \tag{6}$$

σ being the Boltzmann constant, R_{Sun} the radius of the sun and T the temperature of the black body. In a distance D from the sun the irradiance declines as the area grows to $4\pi D^2$. This leaves a total irradiance H_0:

$$H_0 = \frac{R_{\text{Sun}}^2}{D^2} \cdot \sigma T^4 \tag{7}$$

With this model the irradiance received at Vesta and Ceres are calculated.

5 Results

5.1 Coordinate Calculation

The SPICE extension for Matlab (Mice) was used to calculate position and orientation data of DAWN for a given time. A Matlab function was written for this purpose, which works with the appropriate kernels loaded. These kernels are kernels acquired by the DAWN mission as well as kernels by NAIF regarding ancillary data about reference frames, time and movement of solar system bodies (Earth, Vesta, Ceres, Sun). Also, the leap-seconds, that were introduced after the J2000 epoch had to be included in a kernel. With this information the trajectory of DAWN could be calculated and plotted (fig. 15).
The positions of all bodies were calculated in the Vesta-fixed frame and Ceres-fixed frame, respectively. For Vesta the coordinate system Dawn-Claudia was chosen. For correct orientation of the FC, the DAWN reference frame had to be considered. Line-of-sight of the cameras is defined in Z-direction in the DAWN frame. By calculating Euler angles (rotation around the axes Z,Y,Z in this order) the correct camera roll angle could be determined. However, the camera simulation always produced a mirrored picture. The reason for this has to lie in the camera simulation as it is mirrored along the horizontal axes in the centre of the picture.
The line to the sun is another essential part of the simulation. Therefore, this was calculated as well. It is in this case necessary to point out the difference between the geometric position of the sun and the visible direction of the sun. This is due to the time for the light to reach Vesta or Ceres. During this time, the sun has moved in relation to the bodies. For the calculation the visible direction is used, as it is the direction, from which the solar irradiation arrives at the body. Table 4 shows the sun distance for each body at the times of Cycle 1 of the Survey and the light time. As one cycle spans less than 24 hours, the approximate times in minutes is accurate enough to cover the entire cycle.

5.2 Vesta Results

First of all it was tested whether the calculated data was correct. Spacecraft position and camera orientation were calculated and 3D-plotted for phases of HAMO, LAMO and Survey (fig. 16). The calculation and plot were done in the J2000 frame, the position data can therefore be seen as consecutive. As the graphic shows, the movement of the spacecraft is around Vesta, and the orientation of the camera is towards Vesta. In other cases, where no pictures where taken from DAWN but the other instruments are used, the pointing of the camera does not show in the direction of Vesta. The calculation of position and orientation of the camera can therefore be expected to be correct. 116 Pictures were used for the optimization. These are all pictures taken in clear filter during Cycle 1. To show the results of the Optimization figure 17 displays two examples comparing

Body	Distance to Sun	Light Time	Solar Irradiance
Vesta	$336 \cdot 10^6$ km	19 min	256.36 W/m^2
Ceres	$437 \cdot 10^6$ km	24 min	151.55 W/m^2

Table 4: Sun Distance, light time and solar irradiance of Vesta at 11th August 2011 and Ceres at 5th June 2015

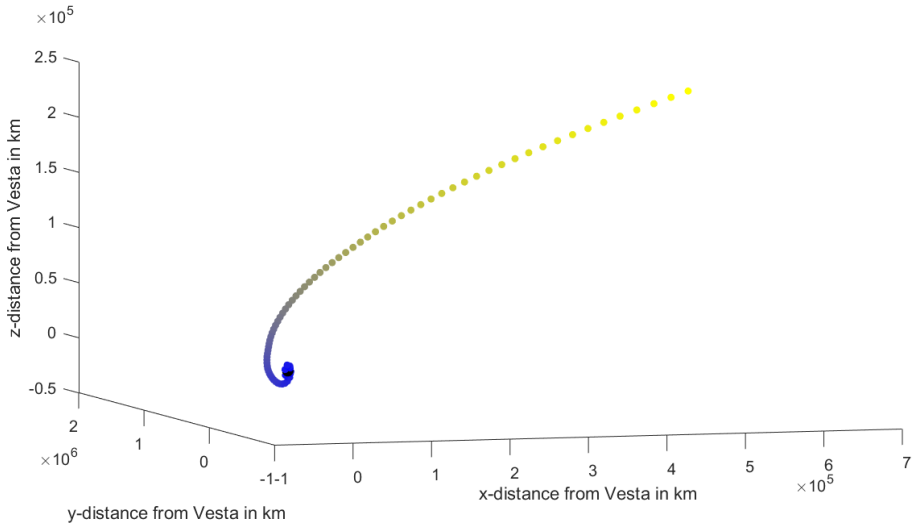

Figure 15: The DAWN approach to Vesta between 1st May 2011 and 1st August 2011 from SPICE data. Vesta lies at (0,0,0).

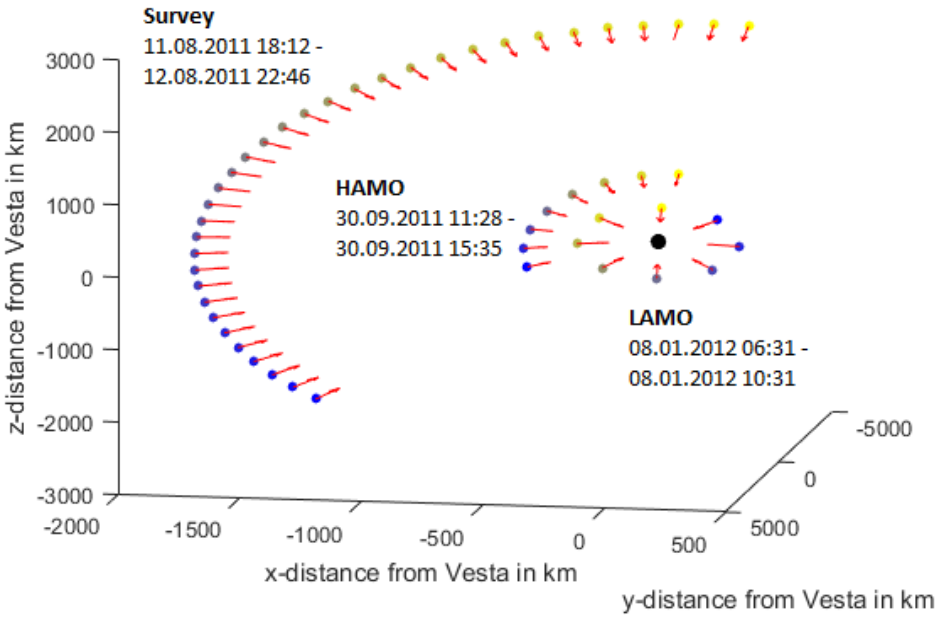

Figure 16: Movement of DAWN in the J2000 reference frame and camera orientation in Survey, HAMO and LAMO orbits around Vesta as extracted from SPICE data. The colours account for the time development (yellow = early, blue = late).

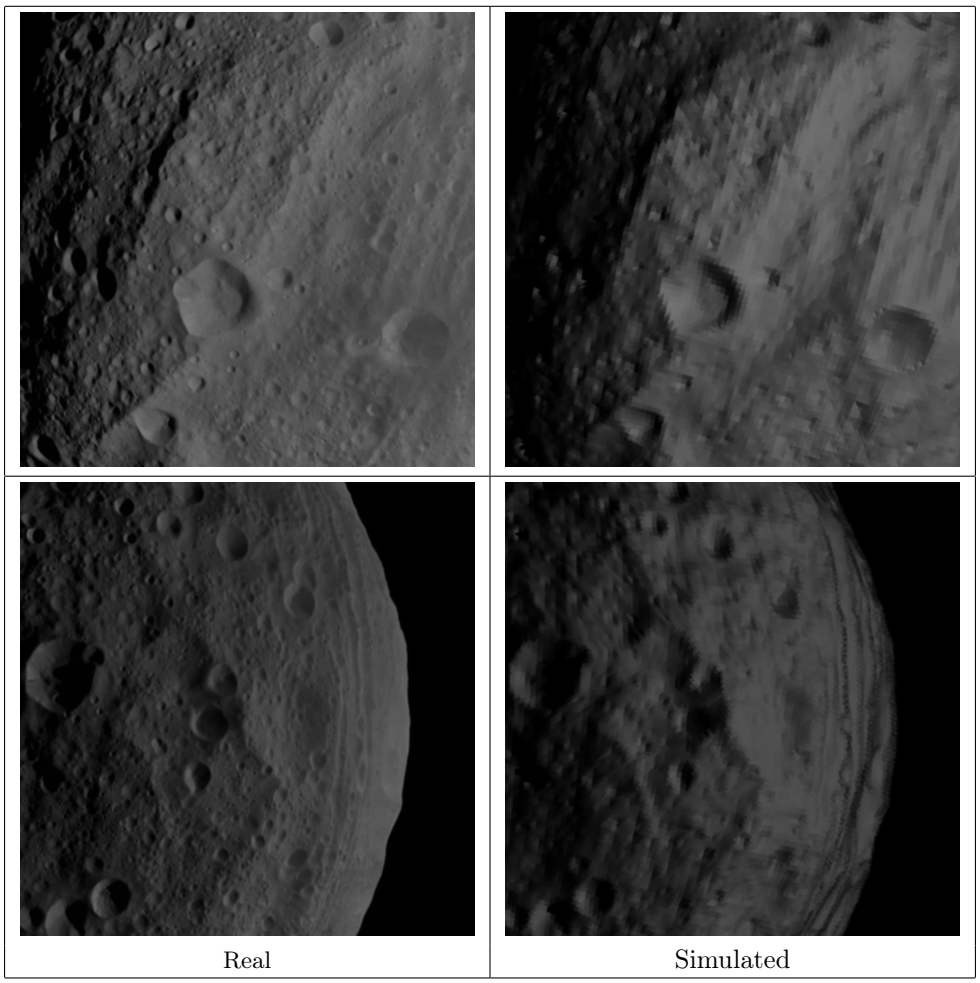

Figure 17: Vesta: Snapshot by DAWN with full 1024x1024 resolution and applied mean filter (left); Simulated picture of a 196608-triangle-model of Vesta with 1024x1024 resolution, applied mean filter, and Hapke-parameters optimized(right)

the real pictures by DAWN to the simulated pictures. It shows that the accuracy of light and shadow in craters is very high, however the contrast in the simulated picture seems to be stronger than in the real picture. This might be a result of the left-out surface roughness in the Hapke-model. Also, the edge of Vesta against the sky is a lot brighter in the real picture than in the model. To test the accuracy of the simulation the proportion of irradiance arriving at Vesta to flux received at the camera (I/F) was calculated with the real data and the simulated data (fig. 18). An expected linear correlation can be found. However, for low phase angles and high I/F values the deviation increases.

For each picture, the optimal Hapke-Parameters resulting in the lowest Z were calculated as described in section 4.4 . The optimal parameters of all pictures were then compared by the statistical mean and standard deviation (1-σ). The results can be found in Table 5 compared to results of other works. The calculated parameters are mean parameters regarding wavelength. In reality the parameters can be wavelength-dependant.

A higher accuracy would be achieved by including many more pictures in the process. This was not

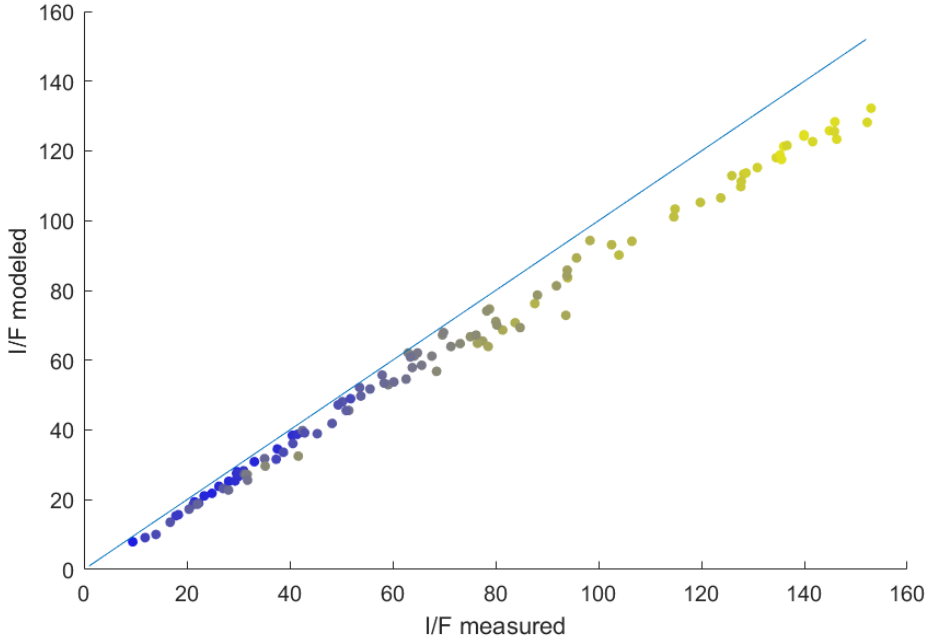

Figure 18: Comparison of real and measured I/F showing linear correlation, although with a slope below the theoretically expected slope of 1. Each data point represents the compared mean values of one picture. The colours indicate the phase angles (yellow=low, blue=high).

	This work	Li et al. (2013)	Hicks et al. (2014)
ω	0.45 ± 0.12	0.51	0.51
g	-0.35 ± 0.22	-0.24	-0.26
B_0	1.83 ± 0.22	1.7	1.0
h	0.53 ± 0.17	0.07	0.098

Table 5: Hapke-parameters compared to the results of other works

possible for this work as the optimization of one picture lasted about 5 hours. However, the resulting parameters ω and g are in the same error margin as in [13] and [3] depicted.
B_0 is higher than the theoretically expected maximum of 1.0. This phenomenon occurs in other works for other objects as well and leads to values exceeding 4.0. The reason assumed for this is that the Coherent Backscatter Opposition Effect (CBOE) is not regarded in these models [13].
The h-parameter is very unusual, as the best approximation is entirely different from results of other work. As h defines the hot spot width, it is the parameter with the smallest influence on Z, hence it is very difficult for an inverse model to extract the correct parameter and it might be inaccurate in this work. Realistic values are $h = 0.07 \pm 0.03$.
Especially ω was also expected to be the most stable variable, as its value is effectively multiplied to every other function in the Hapke-model (eq (1)). Therefore every change in its value changes the value of the phase function significantly. This does not apply to B_0 and h. These parameters are only included in the hot-spot correction function and seem to be dependant of each other. It was tested how a change of the h-parameter determines the result of Z and it was found that even vast differences in h have almost no significant influence on Z. The same test for B_0 gives a similar result. It can be assumed, that the optimization method was not suitable to find the optimal hot-spot parameters.

The work of Li et al. (2013) [13] uses a slightly different approach to this work. The Hapke model includes the macroscopic surface roughness parameter Θ. This is another variable in the model which makes it a five-parameter problem. In addition to this a Minnaert model is also used. With both different models a detailed photometric analysis was done based on the images by the DAWN Framing Camera. The approaches were made with a Disk-integrated phase function, which means that the total flux of reflected light is measured before the object fills the field-of-view, and a disk-resolved phase function, which compares the measured intensity from Vesta for each pixel with the incident solar irradiance. The Hapke-model itself was extracted from [8] and used a single-term Henyey-Greenstein phase function as in this work. DAWN data was used from the approach and survey phase with phase angles from $10 - 80\,^\circ$. The approach data however did not cover this range. The RC3 and RC3b images covered phase angles $30 - 40\,^\circ$ and $5 - 15\,^\circ$, respectively. As the amount of data points in total was a lot higher, this was not assumed a problem. The total range of phase angles used are therefore almost identical to this work. The Hapke-parameters are given in a much smaller error margin. However, the errors especially for the hot-spot parameters were difficult to estimate here as well, as significantly different values for B_0 led to only slightly different results in Z. It is therefore assumed that the hot-spot parameters could not be well-constrained. In addition to finding the Hapke-parameters for the clear filter, Li et al. found the parameters for all filters. The results are that only the SSA shows a significant dependence on wavelength (fig 19). The optimization was done with the global optimization algorithm MPFIT, and to avoid local minima at least 100 randomly chosen different starting values were used.

The work of Hicks et al. (2014) [11] was done with ground-based observation and full-disk observations from DAWN. Without the DAWN data a fit was performed for the Hapke-model and a a mean normalization factor was found to bring the DAWN data points in line. The phase angles used were

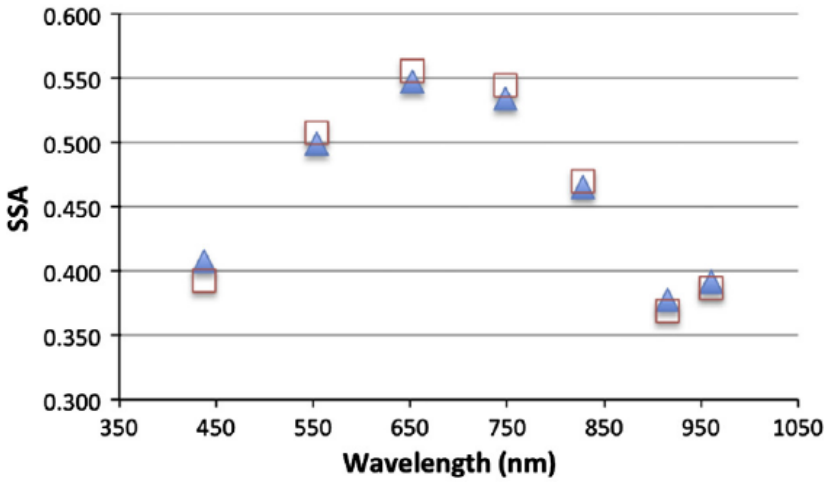

Figure 19: Wavelength dependant SSA, results and reprint from [13]

in the range of 29 ° to 44 °. The Hapke-model in this case was the same as in the work of Li et al. It is not clearly stated whether the value for B_0 was limited to a maximum of 1.0. Also, no error margin or discussion is presented.

The best fit for Z shows an interesting dependence on the phase angle (fig. 20). For phase angles between 45°and 80° the values for Z are significantly higher than in most cases for angles in between 10° and 45°. This contradicts the assumption of accuracy being best at high phase angles as figure 18 indicates.

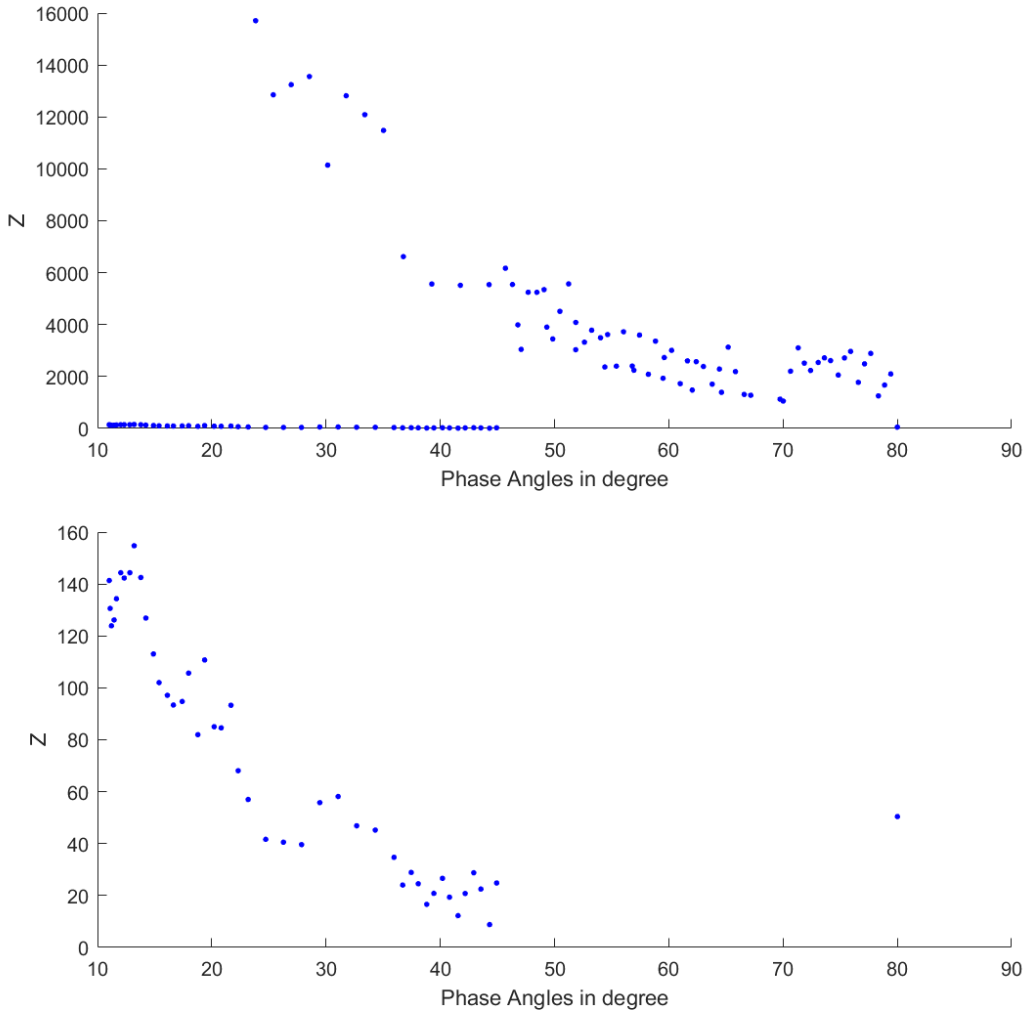

Figure 20: Results for Z over phase angles. The best results for Z could be found at phase angles around 45°.

5.3 Ceres Results

For Ceres the calculated coordinates and camera orientation were tested as well and showed the expected orientation. The process of finding the Hapke-parameters was similar to the process at Vesta. However, the optimization had severe difficulties in finding the optimal values. This was made clear as the optimal values for g always turned to -0.99 or 0.99 which were the boundaries given. These values are for the P-function of the Hapke-model (1) not surprising, as P minimizes for $g = -1$ and $g = 1$ for all phase angles (fig. 21). The reason for this being significant at Ceres but not at Vesta is probably the very low SSA, hence the low influence of ω in the phase-function. To get better values for g the boundaries were changed to $g_{\min} = -0.8$ and $g_{\max} = 0.8$. Additionally the hot-spot parameters were fixed to values $B_0 = 1.6$ and $h = 0.059$ gained from other work [26]. This did not change the problem of an unconstrained g. The only parameter extracted with our optimization process is the SSA. This lies at

$$\omega = 0.020 \pm 0.005$$

with the error being the 1-σ error. This value for ω is very low and slightly below the value found in other work, for example [9] finds a value of $\omega = 0.057 \pm 0.004$.

Another reason for this calculation to be not as accurate as in Vesta for most parameters is the use of the triangular grid of Ceres. An alpha-version was used instead of the hugely improved and updated Vesta model. Also larger size of Ceres has an influence as the triangular grid with the same amount of triangles as the Vesta grid has to cover a much larger area. Hence, the resolution of Ceres is not as high. Also, there is a slight derivation in orientation as can be seen in the pictures (fig. 22. This has an influence on the optimization as the pixels are compared one by one. It was tried to solve this problem by reducing the resolution of the pictures but this did not lead to improved results.

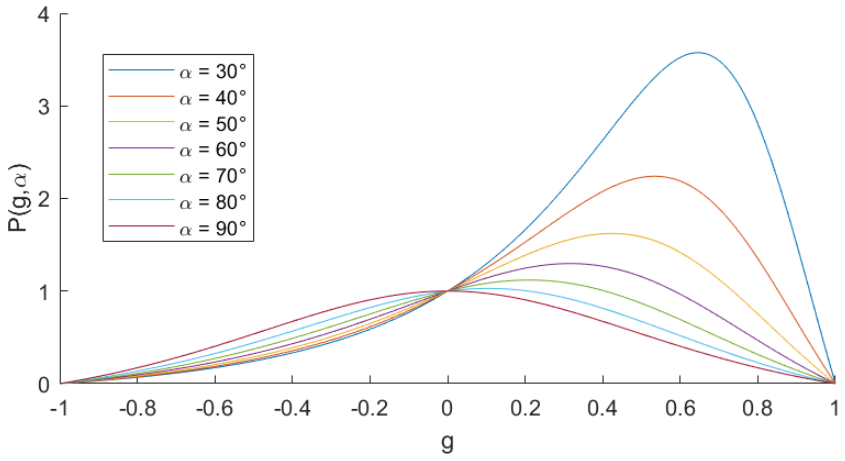

Figure 21: The Henyey-Greenstein phase function P over g for different phase angles α.

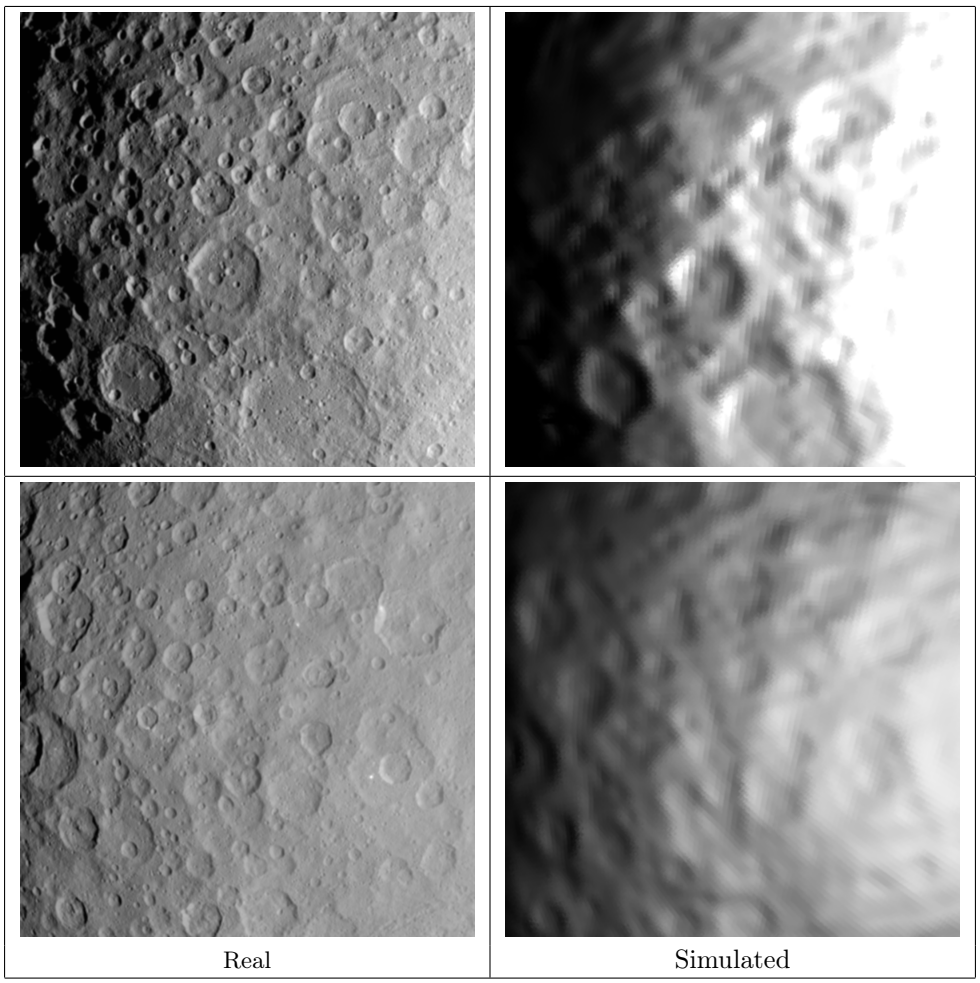

Figure 22: Ceres: Snapshot by DAWN with full 1024x1024 resolution and applied mean filter (left); Simulated picture (right) of a 196608-triangle-model of Ceres with 1024x1024 resolution, applied mean filter, and Hapke-parameters optimized

6 Conclusion & Outlook

The Hapke-parameters were determined with disk-resolved photometric analysis for Vesta and Ceres. For coordinate calculation SPICE was used, an illumination and camera simulation produced simulated pictures and in an optimization process comparing real and simulated picture the Hapke-parameters were determined. For Vesta, the results were $\omega = 0.45 \pm 0.12$, $g = -0.35 \pm 0.22$, $B_0 = 1.83 \pm 0.22$ and $h = 0.53 \pm 0.17$. The results of the SSA, g and B_0 are in accordance to the results of other work. However, the hot-spot parameters are not well constrained, which the result for h shows. This problem is not singular to this work but is a problem of the Hapke-model itself. For Ceres only the SSA could be determined with $\omega = 0.020 \pm 0.004$. This is probably due to the low albedo and the strong dependence on the other values.

In the way that this optimization process is programmed, it would be easy to examine other asteroids, but also Mercury or Pluto could be subject to a similar work. The only problem is the long calculation time. Therefore, an implementation of a more efficient optimization process would improve the quality of the program significantly. Also the solar irradiance is dependant on the wavelength of the light and the Hapke-Parameters are dependant on wavelength. As data about solar irradiance is only available for Earth, this could be used and scaled to the distance of the examined object from the sun.

References

[1] John King-Tai Au. "An Ab Initio Approach to the Inverse Problem-Based Design of Photonic Bandgap Devices". PhD thesis. California Institute of Technology, 2007.

[2] C. R. Chapman, D. Morrison and B. Zellner. "Surface properties of asteroids - A synthesis of polarimetry, radiometry, and spectrophotometry". In: *Icarus* 25 (May 1975), pp. 104–130. DOI: 10.1016/0019-1035(75)90191-8.

[3] Michael D. Hicks et al. "Spectral diversity and photometric behavior of main-belt and near-Earth vestoids and (4) Vesta: A study in preparation for the Dawn encounter". In: 235 (Feb. 2014), pp. 60–74.

[4] DLR. *Dawn mission instruments*. 2012. URL: http://www.dlr.de/dlr/en/desktopdefault.aspx/tabid-10558/965_read-2019#/gallery/3894 (visited on 29th Sept. 2017).

[5] Heiz-Werner Engl, Martin Hanke and Andreas Neubauer. *Regularization of Inverse Problems*. Springer Netherlands/Kluwer Academic Publishers, 2000. ISBN: 978-0-7923-4157-4.

[6] ESA. *Mission information*. 2017. URL: http://sci.esa.int/rosetta/ (visited on 29th Sept. 2017).

[7] Dongsuk Han et al. "Orbit Transfers for Dawn's Ceres Operations: Navigation and Mission Design Experience at a Dwarf Planet". In: *Space Ops 2016 Conference* (2016). DOI: https://doi.org/10.2514/6.2016-2427. URL: https://arc.aiaa.org/doi/10.2514/6.2016-2427.

[8] Bruce Hapke. *Theory of Reflectance and Emittance Spectroscopy*. Cambridge University Press, 2012. ISBN: 9780521883498.

[9] Paul Helfenstein and J Veverka. "Physical characterization of asteroid surfaces from photometric analysis". In: (Feb. 1989).

[10] L. G. Henyey and J. L. Greenstein. "Diffuse radiation in the Galaxy". In: *Astrophysical Journal* 93 (Jan. 1941), pp. 70–83. DOI: 10.1086/144246.

[11] M. D. Hicks et al. "Spectral diversity and photometric behavior of main-belt and near-Earth vestoids and (4) Vesta: A study in preparation for the Dawn encounter". In: *icarus* 235 (June 2014), pp. 60–74. DOI: 10.1016/j.icarus.2013.11.011.

[12] Jian-Yang Li and Joseph N. Mafi. *Body-Fixed Coordinate Systems for Asteroid (4) Vesta*. 2013. URL: https://sbn.psi.edu/archive/dawn/fc/DWNVFC2_1A/DOCUMENT/VESTA_COORDINATES/VESTA_COORDINATES_131018.PDF (visited on 13th Sept. 2017).

[13] Jian-Yang Li et al. "Global photometric properties of Asteroid (4) Vesta observed with Dawn Framing Camera". In: *Icarus* 226.2 (2013), pp. 1252–1274. ISSN: 0019-1035. DOI: http://dx.doi.org/10.1016/j.icarus.2013.08.011. URL: http://www.sciencedirect.com/science/article/pii/S0019103513003497.

[14] F Marzari et al. "Origin and evolution of the Vesta asteroid family". In: 316 (Nov. 1996), pp. 248–262.

[15] NAIF/NASA. *SPICE*. URL: https://naif.jpl.nasa.gov/naif/index.html (visited on 26th Sept. 2017).

[16] NAIF/NASA. *SPICE Documentation*. URL: https://naif.jpl.nasa.gov/pub/naif/toolkit_docs/Tutorials/pdf/individual_docs/03_spice_overview.pdf (visited on 25th Sept. 2017).

[17] NASA. *4 Vesta: In Depth*. URL: https://solarsystem.nasa.gov/planets/4vesta/indepth (visited on 27th Sept. 2017).

[18] NASA. *Asteroids (from the NEAR press kit)*. URL: https://nssdc.gsfc.nasa.gov/planetary/text/asteroids.txt (visited on 25th Sept. 2017).

[19] NASA. *New Horizons: The First Mission to the Pluto System and the Kuiper Belt*. 2017. URL: https://www.nasa.gov/mission_pages/newhorizons/overview/index.html (visited on 29th Sept. 2017).

[20] NASA/JHUAPL. *Spitzer Surveys Dozens of Near-Earth Asteroids*. URL: https://www.nasa.gov/mission_pages/spitzer/multimedia/eros.html (visited on 25th Sept. 2017).

[21] NASA/JPL-Caltech/UCAL/MPS/DLR/IDA. *Full View of Asteroid Vesta*. 2017. URL: https://www.nasa.gov/mission_pages/dawn/multimedia/pia15678.html (visited on 13th Sept. 2017).

[22] NASA/JPL-Caltech/UCLA/MPS/DLR/IDA. *'Bright Spot' on Ceres Has Dimmer Companion*. 2015. URL: https://www.nasa.gov/jpl/dawn/bright-spot-on-ceres-has-dimmer-companion (visited on 25th Sept. 2017).

[23] NASA/JPL/JHUAPL. *Asteroid Mathilde*. URL: https://solarsystem.nasa.gov/galleries/asteroid-mathilde (visited on 25th Sept. 2017).

[24] NOAO. *Asteroid Spectra*. URL: http://www.observeasteroids.org/images/spectra2.gif (visited on 29th Sept. 2017).

[25] Nola T. Redd. *Vesta: Facts About the Brightest Asteroid*. 2015. URL: https://www.space.com/12097-vesta-asteroid-facts-solar-system.html (visited on 27th Sept. 2017).

[26] V. Reddy et al. "Photometric properties of Ceres from telescopic observations using Dawn Framing Camera color filters". In: *icarus* 260 (Nov. 2015), pp. 332–345. DOI: 10.1016/j.icarus.2015.06.039. eprint: 1510.00387 (astro-ph.EP).

[27] Schroder and J. Mafi. *Instrument information*. 2012. URL: https://sbn.psi.edu/archive/dawn/fc/DWNVFC2_1A/CATALOG/fc2_instrument.cat (visited on 29th Sept. 2017).

[28] H. Sierks et al. "The Dawn Framing Camera". In: *Space Science Reviews* 163.1 (Dec. 2011), pp. 263–327. ISSN: 1572-9672. DOI: 10.1007/s11214-011-9745-4. URL: https://doi.org/10.1007/s11214-011-9745-4.

[29] Tahc. *Euler diagram showing the types of bodies in the Solar System*. 2015. URL: https://en.wikipedia.org/wiki/Small_Solar_System_body#/media/File:Euler_diagram_of_solar_system_bodies.svg (visited on 12th Sept. 2017).

[30] D. J. Tholen and M. A. Barucci. "Asteroid taxonomy". In: *Asteroids II*. Ed. by R. P. Binzel, T. Gehrels and M. S. Matthews. 1989, pp. 298–315.

[31] International Astronomical Union. *Definition of a Planet in the Solar System*. Resolution GA26-5-6. 2006.